Conditions of Mélange Diapir Formation

Cristy Q. Ho

GEOL394

Fall 2019

Advisors: Dr. Sarah Penniston-Dorland, Kayleigh Harvey, and Dr. Laurent Montési

Abstract

Subduction zones are regions where volatiles, sediments, crustal rocks, and mantle rocks are recycled in the interior of the Earth. The flux of materials affects the composition of the mantle and of lavas that erupt to create volcanic arcs. This flux can be constrained by studying the physical and chemical properties of rocks within subduction zones. Mélange, a heterogenous mixture of sedimentary, mafic, and ultramafic rocks is found at exhumed subduction interfaces and is interpreted to be exhumed from the region where the subducting slab is in contact with the overlying mantle wedge. Some studies suggest that mélange detaches from the subduction interface and rises as a diapir. The process of mélange diapir formation has implications for affecting the flux of material from the mantle to the Earth's surface. This is because slab material that rises to form diapirs may be a potential source of magma for volcanic arcs. The goal of this project was to determine the conditions under which mélange diapirs could form at the subduction interface and assess whether these conditions are realistic for subduction zones. This was determined by calculating the density contrast between the mantle wedge and mélange material, and by considering the effect of subduction rate on diapir formation and stability. A diapir will grow where there is a negative density contrast, where material at the slab interface is less dense than the overlying mantle wedge. However, a diapir will not form if the velocity of the subducting slab is too fast relative to the growth rate of the diapir. In this project, the likelihood of mélange diapir formation was determined by calculating densities over a range of pressure and temperature conditions based on the compositions of samples taken from exhumed mélange. Three samples were collected from an exhumed subduction interface located on Santa Catalina Island, California. One sample of serpentinite represents the metasomatized mantle wedge, whereas the other two samples each represent a different composition of mélange. Petrography and electron probe microanalysis (EPMA) were completed to assess mineral assemblages and X-ray fluorescence (XRF) analysis was performed to determine the bulk chemical composition of each sample. The mineralogical and geochemical data were used to create forward thermodynamic models with the program Perple_X in order to calculate how rock density changes along the slab interface. P-T conditions where there is a negative density contrast between mélange material and the mantle wedge were used to create geodynamic models of mélange diapir formation. Density contrasts were calculated along slab pressure and temperature paths of Central Cascadia, a hot subduction zone analogous to that of the Catalina Schist. Generally, there was no negative density contrast except for at 644 – 676 °C and 2.3 – 2.4 GPa between the pyroxene-rich matrix and the serpentinite. However, the smallest diapir growth time was calculated to be 0.83 Ma, which is greater than 0.41 Ma, the calculated slab time. According to the results, mélange cannot rise to form a diapir because the subducting slab is too fast and would entrain the region of negative density contrast.

Introduction

The recycling of materials from the Earth's surface into the mantle occurs at subduction zones (Nielsen and Marschall, 2017). These materials include water, carbon dioxide, and sediments, as well as rocks from the oceanic crust and serpentinized mantle. These materials can all be found at the subduction interface, the region where the subducting slab is in contact with the overlying mantle wedge. Exposures of exhumed subduction interfaces reveal that sediments, oceanic crustal rocks, and serpentinized mantle rocks are mixed in regions called mélange zones and that mélange exists at the subduction interface (Bebout and Penniston-Dorland, 2016). Mixing and melting processes within subduction zones are not fully understood and are difficult to study due to a scarcity of exhumed subduction interfaces (Bebout and Barton, 2002). The type of chemical reactions that occur at subduction zones are controlled by changes in temperature and pressure conditions with depth. The addition or removal of chemical constituents such as water and carbon dioxide through reactions can alter oceanic crust and metasomatize the surrounding mantle. Water released through dehydration reactions may lower melting temperatures and generate magma. According to the metasomatized mantle wedge melting model (Figure 1A), melt production in volcanoes can be explained by the rising of aqueous fluids and melts derived from the slab (Marschall and Schumacher, 2012). It has been proposed in the mélange diapir model (Figure 1B) that slab materials physically mix to form mélange and detach from the subduction interface to form a diapir, which then rises through the overlying mantle wedge, providing a potential source of magma for volcanic arcs (Marschall and Schumacher, 2012).

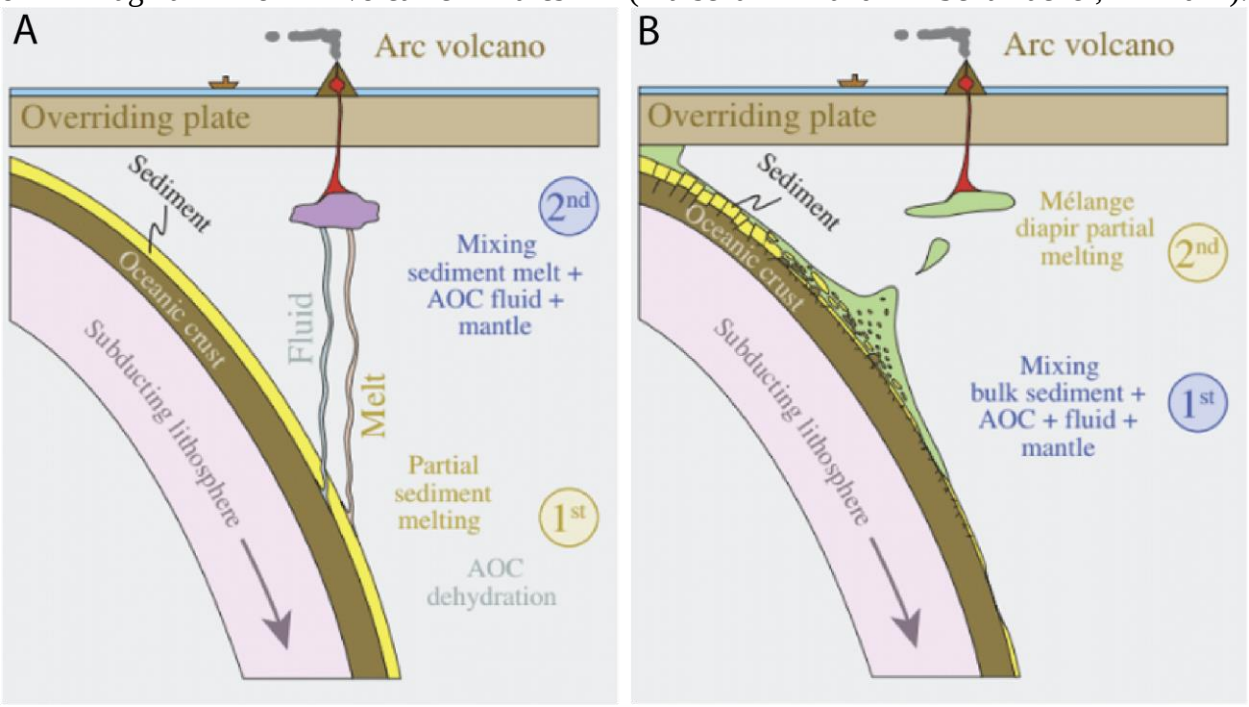

Figure 1: Two end-member models for arc magma generation of metasomatized mantle wedge melting and mélange diapir melting (Nielsen and Marschall, 2017). Ultimately, mixing and melting is reversed for the two end-member models. In the metasomatized mantle wedge melting model (A), melting occurs before mixing, whereas mixing occurs before melting in the mélange diapir model (B).

The metasomatized mantle wedge melting model is more established than the diapir melting model. However, the latter is worth considering because it is compatible with geochemical data

that suggest that trace elements are retained at the cool slab interface and are released when they rise and melt, which is consistent with the formation of high-pressure mélange before the generation of arc magmas (Marschall and Schumacher, 2012). Some geochemical signatures, such as the enrichment of Rb, Sr, LREE (Light Rare Earth Elements) and other large-ion-lithophile elements of island-arc basalts can be explained by the incorporation of slab materials (McCulloch and Gamble, 1991). Remaining slab materials descend and contribute to the heterogeneity of the mantle, causing the wide variability in the major element, trace element, and isotopic compositions of ocean-island basalts (Weaver, 1991). Arc magma generation can be caused by varying degrees of both metasomatized mantle wedge melting and diapir melting. Thus, determining the specific styles of arc magma generation has implications for constraining the amounts of chemical constituents that escape or are stored in the mantle.

Subduction zone processes must be considered when determining the flux of water between the mantle and the surface. The amount of water retained by the subducting slab affects the viscosity and rate of cycling in the mantle, which affects the movement of tectonic plates. Subducting slabs can completely dehydrate at shallow depths in hot subduction zones, whereas water can be retained at depths down to the lower crust and upper mantle in cold subduction zones (van Keken et al. 2011). Additionally, the water content of a slab is also dependent upon bulk composition. Slab composition, pressure, and temperature control mineral stability, and the ability to structurally store water varies among different minerals. Water that escapes from the dehydrating slab lowers the density of overlying materials, which may rise as a diapir if a sufficient negative density contrast is generated (Hasenclever et al., 2012). Diapirs could rise though the mantle wedge towards the surface and accelerate the cycling of materials that occur at subduction zones. Materials ascending rapidly through connected diapir conduits are consistent with geochemical data of uranium-thorium series disequilibrium, which requires rapid transport between the slab interface and the surface (Hall and Kincaid, 2001). The flux of materials may be further constrained by examining the conditions under which materials will rise from the slab interface to form diapirs.

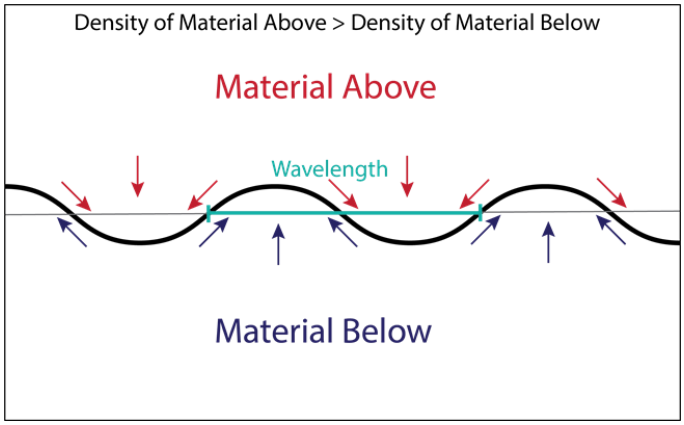

Figure 2: The movement of materials along an unstable interface caused by a negative density contrast.

Diapir formation depends on the interplay of density, viscosity, wavelength of perturbation, and slab velocity (Turcotte and Schubert, 2014). First, a Rayleigh-Taylor instability is required to cause a negative density contrast in which the rising material must be less dense than the overlying material (Figure 2). The density and viscosity of a material are determined by its composition and the pressure and temperature conditions it is subjected to. Thus, density contrast varies along the subduction interface depending on the compositions of the diapir (the rising material) and the mantle wedge (the overlying material). Generally, diapirs are more likely to form from low-density materials, such as sedimentary rocks. Previous geodynamic models have been focused on diapirs derived from sedimentary rocks (Behn et al., 2011) and mafic rocks (Gerya and Yuen, 2003). In this study, diapirs were assumed to be derived from mélange, which has a composition that is distinct from the individual sedimentary,

mafic, and ultramafic components it is derived from. Is it possible for diapirs to form from mélange located at the subduction slab interface? A negative density contrast is just one of the criteria required to cause diapir formation. Viscosity strongly determines the shape and growth rate of diapirs (Zhu et al., 2009). Diapir growth rate and its relation to subduction rate also need to be considered because a plate that is subducting too rapidly will prevent diapir formation even if the required density contrast is present (Miller and Behn, 2012). Therefore, younger and warmer subducting plates which are associated with slower subduction rates have a greater chance of promoting diapir growth.

The purpose of this project was to determine the likelihood of diapir formation from mélange at the subduction interface by integrating four techniques: petrography, geochemical analysis, thermodynamic modeling, and geodynamic modeling. Samples were collected of mélange and mineral assemblages were determined. Thermodynamic models were constructed that best matched the observed mineral assemblages and were then used to predict the mineral assemblages over the range of pressure and temperature conditions expected within the subduction zone. Densities for both mélange and mantle were calculated over a range of pressure and temperature conditions along the subduction interface. These calculations were based on the mineralogical and geochemical compositions of two rocks that each represent a different composition of mélange, and of another rock that represents the metasomatized mantle wedge. Diapir formation was tested by determining the density contrast between mélange at the subduction interface and overlying mantle, as well as by comparing diapir growth time to subduction time. Diapir formation is possible if there is a negative density contrast where mélange is less dense than the overlying mantle. The calculated densities of the samples were used to calculate diapir growth time, which is also affected by viscosity, mélange thickness, wavelength, and subduction rate. These parameters were accounted for in the geodynamic models in order to determine the optimal conditions for diapir formation. The calculated diapir growth time was compared to subduction time to determine if the rise of the mélange diapir is fast enough to overcome entrainment by the mantle.

Geologic Background

The high-pressure metamorphic rocks ranging from blueschist to amphibolite facies are characteristic of the Catalina Schist, an exhumed paleo-subduction zone located on Santa Catalina Island off the coast of California. Peak pressures and temperatures recorded in the rocks are 0.7 – 1.2 GPa and 250 – 750 °C, respectively (Platt, 1976).

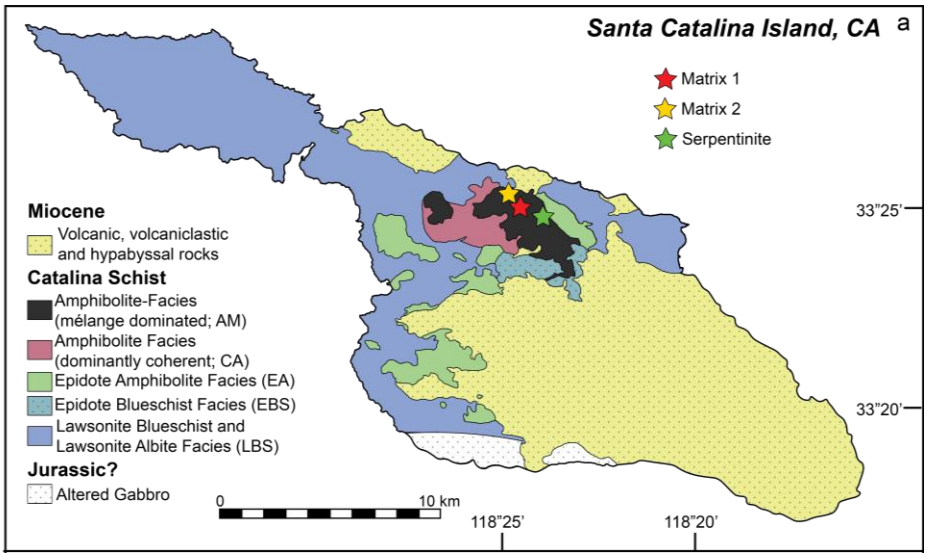

Figure 3: A geologic map of Santa Catalina Island with sample locations marked (Adapted from Platt, 1976).

Of particular interest to this study was the amphibolite unit, which consists of rock types with peak pressure and temperature conditions of 0.8 – 1.1 GPa and 640 – 750 °C (Bebout and Barton, 2002; Sorensen and Barton, 1987; Penniston-Dorland et al., 2018). The amphibolite unit contains metamorphosed ultramafic rocks and mélange consisting of blocks of sedimentary, mafic, and ultramafic rocks surrounded by a finer-grained matrix (Figure 4).

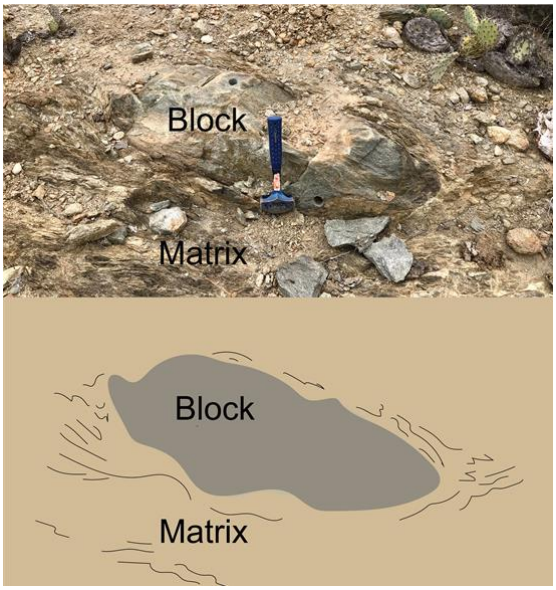

Figure 4: A photo and sketch of metamorphic mélange on Santa Catalina Island, California. This mélange is composed of ultramafic blocks of serpentinite and mafic blocks of garnet amphibolite that are surrounded by a foliated matrix rich in sheet silicates.

Exposures of exhumed subduction interfaces reveal that sediments, oceanic crustal rocks, and serpentinized mantle rocks are mixed in regions called mélange zones (Figure 5) (Bebout and Penniston-Dorland, 2016). The mélange zone of the Catalina Schist is inferred to have experienced kilometer-scale mixing (Bebout and Barton, 2002). Exhumed terranes provide direct access to mélange matrix formed at the slab interface. Samples were collected from the amphibolite unit of the Catalina Schist and were assumed to have formed at the slab interface. One sample of serpentinite was chosen to represent the composition of the metasomatized mantle, and two other samples of mélange matrix were chosen to represent the composition of mélange. The samples that represent mélange have a different composition from one another and were selected to account for different ranges of mineralogical and geochemical compositions found in mélange. In this paper, the chlorite-biotite matrix is referred to as Matrix 1 and the orthopyroxene-rich matrix is referred to as Matrix 2.

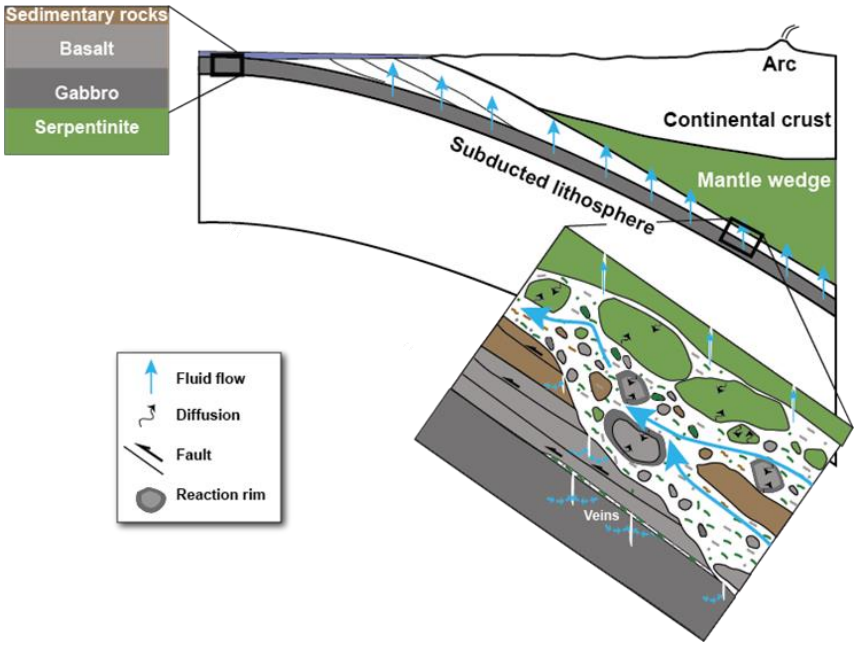

Figure 5: Block-in-matrix model for the origin of mélange in a subduction zone. Blocks of serpentinite, gabbro, basalt, and sedimentary rocks are surrounded by finer-grained materials (Bebout and Penniston-Dorland, 2016).

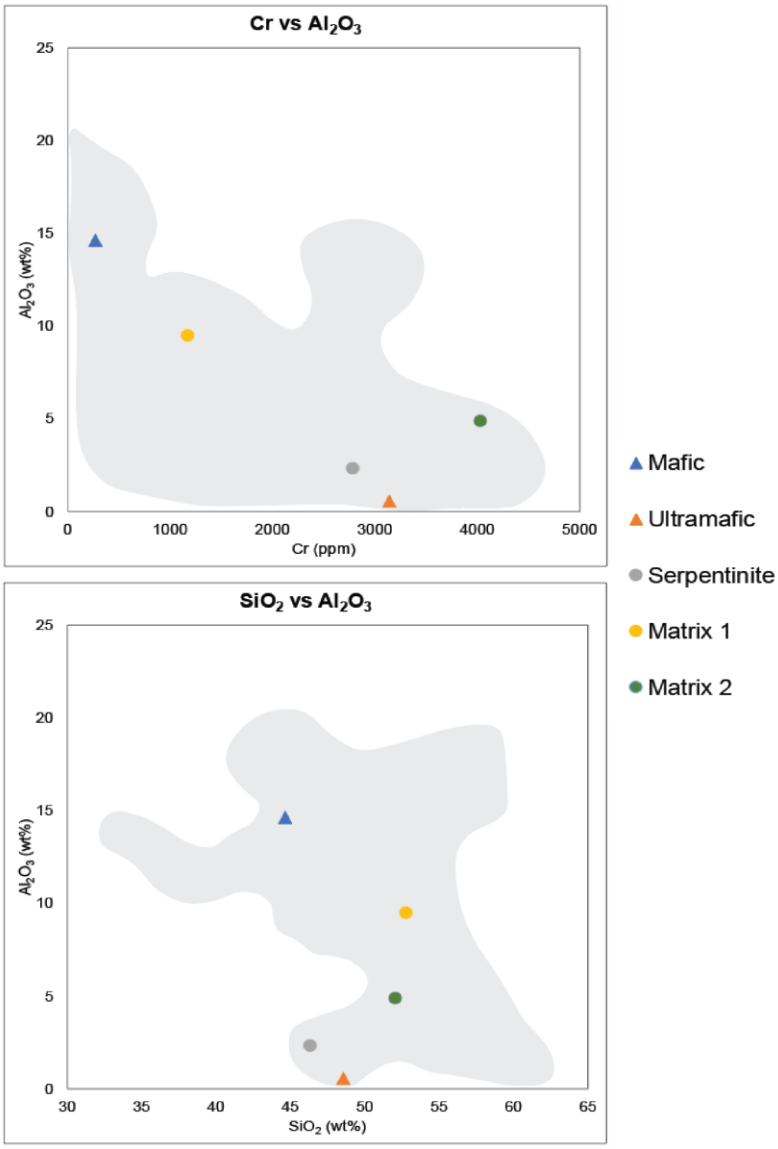

Figure 6: The mean concentrations for mafic and ulframafic rocks as well as the concentrations of the various types of mélange matrix (shaded grey areas) are based on Catalina Schist (Bebout and Barton 2002). Serpentinite, Matrix 1, and Matrix 2 concentrations are from the bulk rock composition data in Table 1A of the Appendix.

The Catalina Schist mélange is rich in Mg and contains varying percentages of talc, chlorite, anthophyllite, calcic-amphibole, and enstatite (Bebout and Barton, 2002). Because mélange is a mixture of different rock types, mélange matrix can vary in composition depending on the degree of mixing and the amount of sedimentary, mafic, and ultramafic materials present. The diverse modal proportions of Al_2O_3 and Cr of mélange as shown in Figure 6 are indicative of various degrees of mixing (Bebout and Barton, 2002). The average mafic rock from the Catalina Schist is rich in Al_2O_3 and depleted in Cr and SiO_2 compared to most of the other samples. The ultramafic rock is depleted in Al_2O_3 and rich in Cr and SiO_2 compared to the mafic rock. The three samples used in this project fall in between the Al_2O_3 and Cr values for the mafic and ultramafic rocks. Serpentinite has similar values to the mean ultramafic rock. The SiO_2 and Al_2O_3 values for Matrix 1 and Matrix 2 are similar to that of the other matrices.

Methodology

Mineralogy

Petrography was used to determine the mineral assemblages of samples collected from a paleo-subduction zone. Observations of mineral assemblages in thin section were used to assess the quality of the thermodynamic models. Mineral abundances were also determined with Adobe Photoshop using the method described in Figure 1 of the Appendix. The observational data were compared to the mineral assemblages predicted by the models. Thin sections of each sample were made. A Nikon Eclipse LV100POL petrographic microscope was used to observe the mineralogical assemblages of each sample. Electron probe microanalysis (EPMA) was performed

on minerals to characterize chemical formulas. The probe was setup to run at an accelerating voltage of 15 kV, a cup current of 20 nA, and a beam diameter of 5 µm. Raw x-ray intensities were corrected with a ZAF algorithm.

Geochemical Analysis

Samples were powdered using an alumina ceramic shatterbox. Powdered samples were sent to Franklin and Marshall College for XRF analysis. XRF analysis was performed using a Panalytical XRF spectrometer to obtain bulk rock composition of samples. Bulk rock composition includes the major oxides in wt% and trace elements in ppm.

Thermodynamic Modeling

The program Perple_X (version 6.8.6; Connolly, 2009) was used together with the Holland and Powell (2011) database to perform calculations. Perple_X uses thermodynamic data to predict stable mineral assemblages over a range of pressure and temperature conditions and was used to calculate how bulk rock density changes along the slab interface. The quality of Perple_X models were assessed by comparing the model output to the observed mineralogy of the samples.

Geodynamic Modeling

Diapir models were constructed based on Perple_X density contrast calculations at pressures between 0 – 4.0 GPa and temperatures between 400 – 1000 °C. Two density contrasts were calculated: the first between Matrix 1 and Serpentinite and the second between Matrix 2 and Serpentinite. Both matrices represent a different composition of mélange and the serpentinite represents the metasomatized mantle (Figure 7). Diapir growth time was calculated by using the calculated density contrasts and by varying viscosity, wavelength, and mélange thickness. Diapir growth time was compared to subduction time to determine if the rise of the mélange diapir is fast enough to overcome entrainment by the mantle.

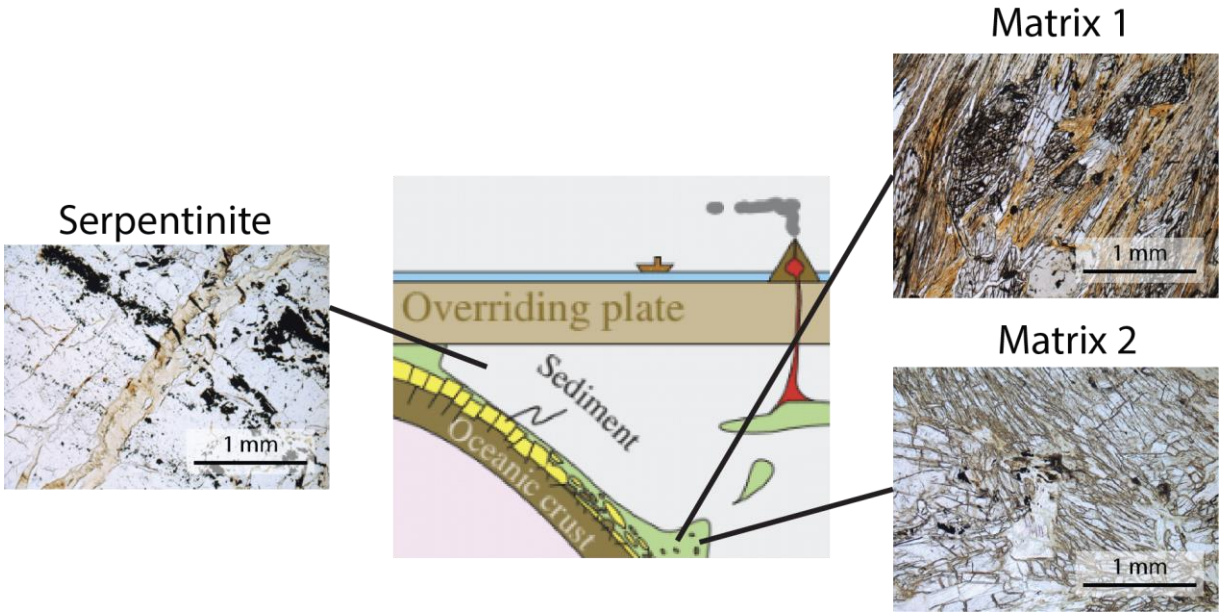

Figure 7: In this experimental design, Serpentinite represents the mantle wedge. Matrix 1 and Matrix 2 represent mélange. The photomicrographs of the samples are in plane-polarized light. The subduction zone image in the center is from Nielsen and Marschall (2017).

Results and Discussion

Mineralogy

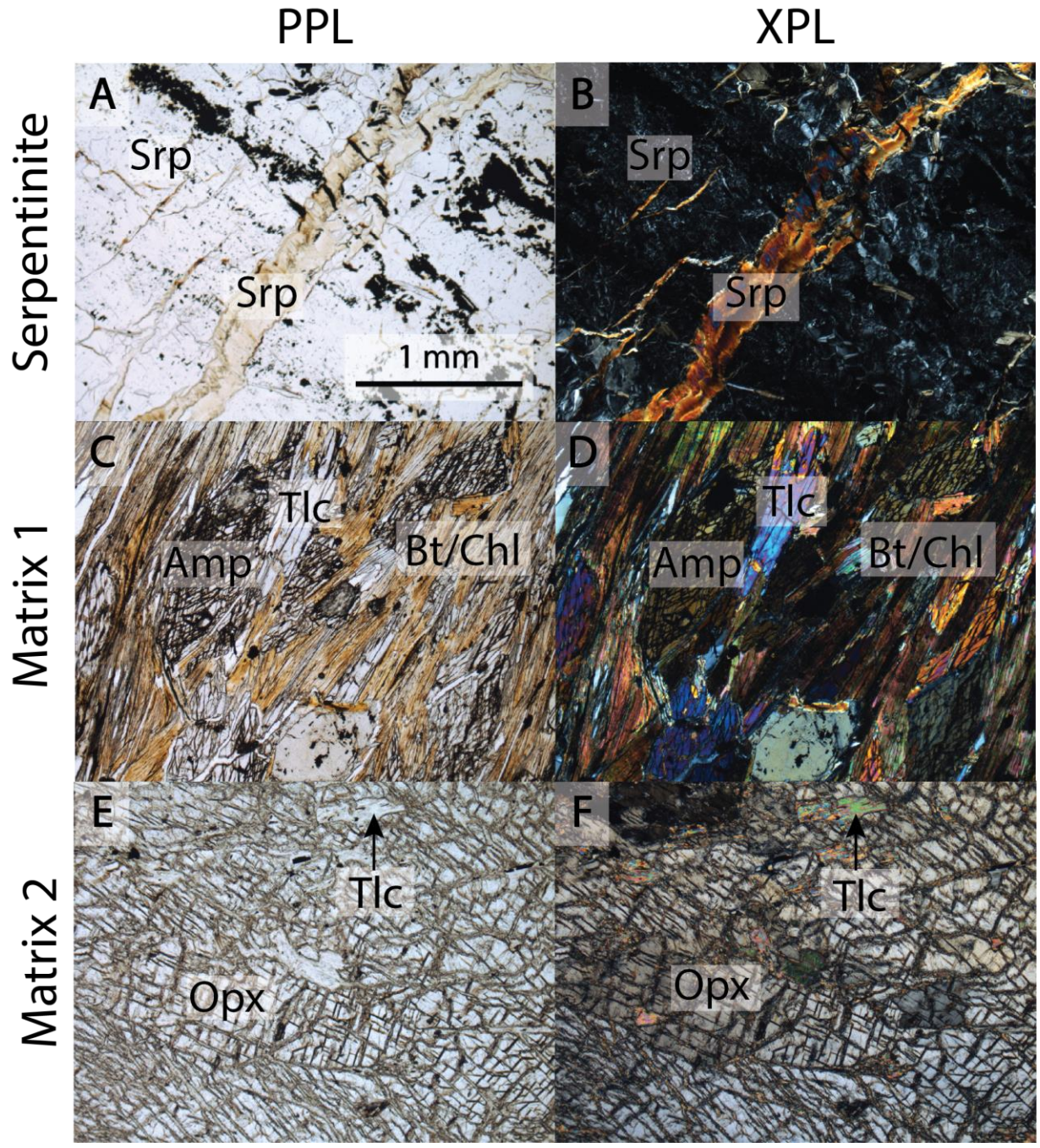

Figure 8: Plane-polarized light (PPL) photomicrographs and cross-polarized light (XPL) photomicrographs of each sample. Mineral abbreviations are derived from Whitney and Evans (2010): Serpentinite (Srp), Amphibole (Amp), Talc (Tlc), Biotite (Bt), Orthopyroxene (Opx)

Serpentinite contains abundant serpentine and the veins within this sample are composed of serpentine as well. There are also olivine pseudomorphs present (Figure 1 in the Appendix) indicating that olivine crystals were serpentinized in the past. Other minerals include chlorite and opaque phases such as hematite and magnetite. Matrix 1 is foliated and abundant in chlorite and biotite (Figure 8). The chlorite and biotite are finely intergrown. Thus, formulas for each mineral could not be calculated from the electron microprobe data. This sample contains magnesiohornblende, a clinoamphibole (Table 1). Talc and quartz are also present. Matrix 2 contains abundant enstatite, an orthopyroxene. The radiating crystal habits indicate that anthophyllite, an orthoamphibole could have once been an abundant mineral. Other minerals in this sample include talc and chlorite. Observed mineral percentages are listed in Table 3.

Mineral Formulas		
Serpentinite	**Matrix 1**	**Matrix 2**
Serpentine $Mg_{2.8}\,Fe_{0.1}\,Si_{2.1}\,O_5(OH)_4$	Talc $Mg_{2.5}\,Fe_{0.3}\,Si_{3.8}\,O_{10}(OH)_2$	Orthopyroxene $Fe_{0.2}\,Mg_{1.8}\,Si_2\,O_6$
Chlorite $Mg_{4.8}\,Fe_{0.2}\,Al_{1.0}\,Si_{3.1}\,Al_{0.8}\,O_{10}(OH)_8$	Magnesiohornblende $Na_{0.2}\,Ca_{1.6}\,Na_{0.4}\,Fe_{0.9}\,Mg_{3.4}\,Al_{1.9}\,Si_{6.9}\,O_{22}(OH)_2$	Talc $Mg_{2.9}\,Fe_{0.1}\,Si_4\,O_{10}(OH)_2$

Table 1: Formulas calculated based on EPMA data (wt% oxides are in Table 3 of the Appendix).

Geochemistry

Whole rock major- and trace-element compositions are listed in Table 1A in the Appendix. To estimate the uncertainty in the XRF analyses, the coefficient of variation was calculated for each major oxide and trace element by calculating the mean and standard deviation of the major oxides and trace elements of various BHVO specimens, which were used as standards. The standard deviation was divided by the mean for each chemical constituent to obtain the coefficient of variation, which are listed in Table 1B of the Appendix. The bulk rock compositions were assumed to be representative of peak metamorphic conditions. Changes in the mobility of elements in a rising diapir due to changes in pressure and temperature conditions were not accounted for in this study.

Thermodynamic Modeling

Serpentinite		**Matrix 1**		**Matrix 2**	
Included Phases	Excluded Oxides	Included Phases	Excluded Oxides	Included Phases	Excluded Oxides
Atg(PN)	CaO	Bio(HP)		Opx(HP)	Na_2O
O(HP)	Na_2O	Chl(W)		Cpx(HP)	
Chl(W)	K_2O	T		T	
Opx(HP)		GlTrTsPg		Chl(W)	
T		Gt(HP)		MF	
MF		Cpx(HP)		Gt(HP)	
IlHm(A)		Opx(HP)		IlHm(A)	
Gt(HP)		IlHm(A)		oAmph(DP)	
		MF		Atg(PN)	

Table 2: Perple_X solution models included and the oxides excluded for each sample model. Phases and references for each solution model are listed in Table 2 of the Appendix.

Solution models that were initially included in Perplex_X models for each sample were associated with minerals observed in thin section. Additional solution models were added to account for solid solutions that appear in P-T regions outside of the expected ranges of 0.8 – 1.1 GPa and 640 – 750 °C, the expected peak conditions. Oxides present in low concentrations (<0.15 wt%) were excluded to allow certain models to run and to create models that were more consistent with observed mineral percentages (Table 3). According to the XRF data (Table 1A of the Appendix), iron is highly oxidized in these samples. Thus, solution models that account for ferric iron and ferrous iron were preferentially used. Mineral abundances predicted by Perple_X for peak metamorphic conditions experienced by samples were compared to the mineral modes of the natural samples to ground truth the models. Serpentinite and Matrix 2 models had mineral assemblages in peak P-T conditions consistent with their respective samples without changing their measured value of iron oxidation. However, the iron oxidation values for Matrix 2 only produce the clinoamphibole observed at less than 0.8 GPa and were not consistent with the assumption that this sample formed at the slab interface. Various alternative solution models were attempted to create a Matrix 1 model with abundant clinoamphibole at 0.8 – 1.1 GPa and 640 – 750 °C. Lowering the iron oxidation was the most effective way of producing the mineral assemblages within peak P-T conditions. Lowering the iron oxidation from the total iron suggested by the XRF data to 5% produced a Matrix 1 model that was the most consistent with observations. One process that can change iron oxidation is oxidation after exhumation during surface weathering. Matrix 2 and Serpentinite could have been oxidized after exhumation as well and were also altered after experiencing peak P-T conditions based on the pseudomorphs observed.

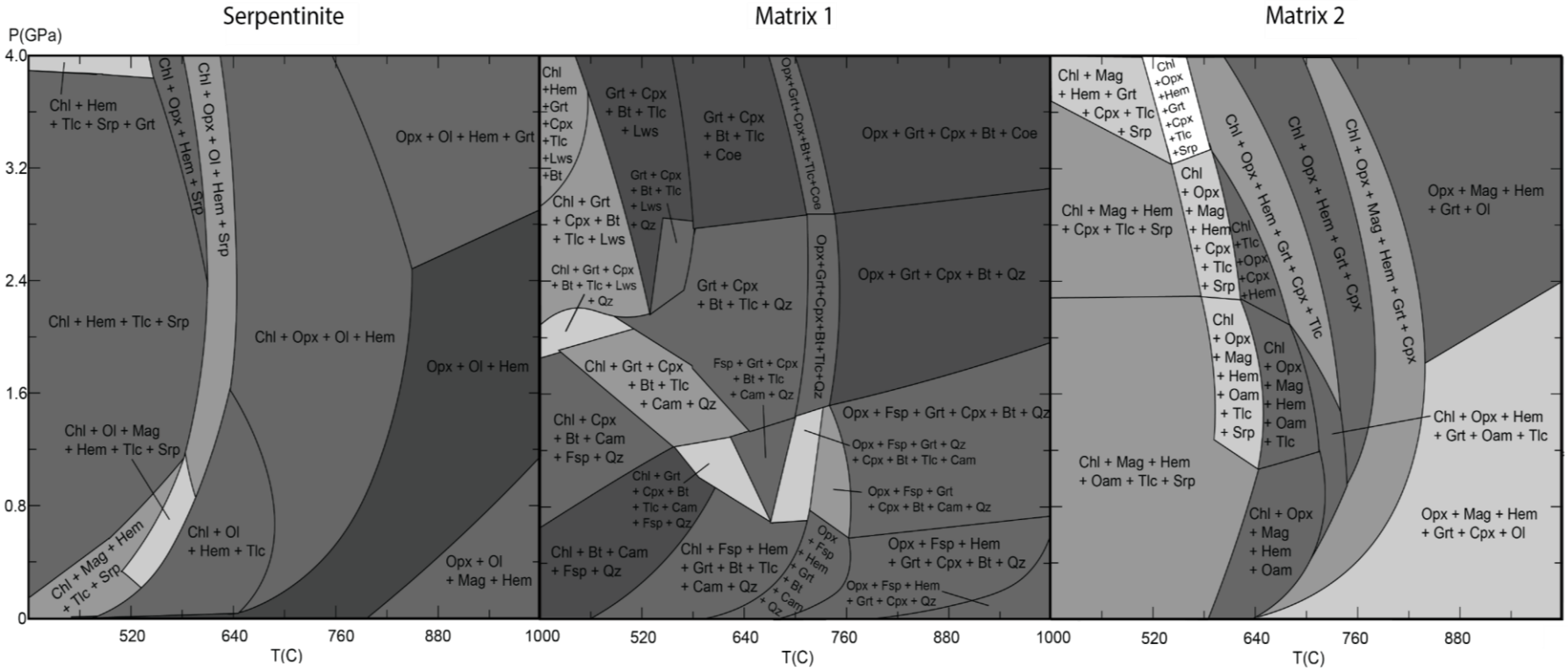

Figure 9: Pseudosections for each of the three samples. Mineral abbreviations from Whitney and Evans (2010): Serpentinite (Srp), Amphibole (Amp), Talc (Tlc), Biotite (Bt), Orthopyroxene (Opx), Chlorite (Chl), Hematite (Hem), Garnet (Grt), Olivine (Ol), Magnetite (Mag), Orthopyroxene (Opx), Clinopyroxene (Cpx), Lawsonite (Lws), Quartz (Qz), Clinoamphibole (Cam), Feldspar (Fsp), Coesite (Coe), Orthoamphibole (Oam)

Pseudosections display the mineral assemblages present in each pressure and temperature field (Figure 9). The pseudosections shown best match the mineral assemblages and abundances in the natural samples. Mineral assemblages vary based on how phase stability is controlled by changing pressures and temperatures. Table 3 is a comparison of the mineral percentages observed and the mineral percentages predicted by Perple_X models for each sample at 600 °C and 700 °C at the same pressure of 1.0 GPa. These temperature and pressure values were chosen based on peak metamorphic conditions expected for matrix belonging to the amphibolite facies (Platt, 1976).

Serpentinite				**Matrix 1**				**Matrix 2**			
Phases	**Observed**	**600 °C**	**700 °C**	**Phases**	**Observed**	**600 °C**	**700 °C**	**Phases**	**Observed**	**600 °C**	**700 °C**
Chl	10%	25%	23%	Chl	30%	32%	0%	Chl	20%	20%	24%
Ol	30% [P]	27%	29%	Hem + Mag	1%	0%	0%	Hem + Mag	1%	2%	2%
Hem + Mag	3%	3%	4%	Grt	0%	1%	14%	Oam	21% [P]	15%	37%
Tlc	0%	25%	0%	Cpx	0%	1%	9%	Tlc	27%	37%	0%
Srp	57%	20%	0%	Bt	20%	8%	7%	Srp	0%	26%	0%
Opx	0%	0%	44%	Tlc	14%	4%	21%	Opx	31%	0%	37%
				Cam	23%	37%	16%				
				Fsp	3%	7%	10%				
				Qz	9%	10%	2%				
				Opx	0%	0%	21%				

Table 3: A comparison of the observed mineral percentages and mineral percentages produced by models at 600 °C and 700 °C for each sample. Percentages of observed pseudomorphs are denoted by [P]. Mineral abbreviations from Whitney and Evans (2010).

Generally, most mineral assemblages predicted by models are consistent with observations. However, there are instances where the models did not replicate the sample mineralogy. The percentage of chlorite observed in thin section was much less than that of the predicted chlorite percentages in the model. Proportions of olivine pseudomorphs were similar to that of the olivine percentages predicted. There was no talc or orthopyroxene observed in thin section or at 700 °C, but were abundant at 600 °C. Serpentine is the most abundant mineral in the sample but was not as abundant in the predicted mineral percentages. A phase transition occurs as temperature increases from 600 °C to 700 °C in the models, where serpentine no longer becomes stable at hotter temperatures and the model becomes dominated by orthopyroxene, olivine, and chlorite. Chlorite and amphibole were abundant minerals observed and predicted at 600 °C for Matrix 2. However, no garnet and clinopyroxene were observed in thin section but ~1% of garnet and ~1% of clinopyroxene were predicted at this temperature. The percentage of biotite and talc were greater in the sample than at 600 °C in the model. Mineral assemblages predicted at 600 °C were more consistent than those at 700 °C, where there was an abundance of garnet and orthopyroxene but no chlorite. Mineral assemblages predicted at 700 °C were more consistent with observed mineral percentages of chlorite, orthopyroxene, and amphibole (including observed pseudomorphs). Models are only as accurate as the assumptions underlying the models, which include the assumption of chemical equilibrium, the assumption that the solution models are all completely accurate for the range of pressure and temperature conditions tested. Heterogeneities in the samples could cause discrepancies between the bulk composition observed in thin section and that of bulk rock XRF data. Each sample has only one thin section which may not fully represent the bulk mineralogy in the samples.

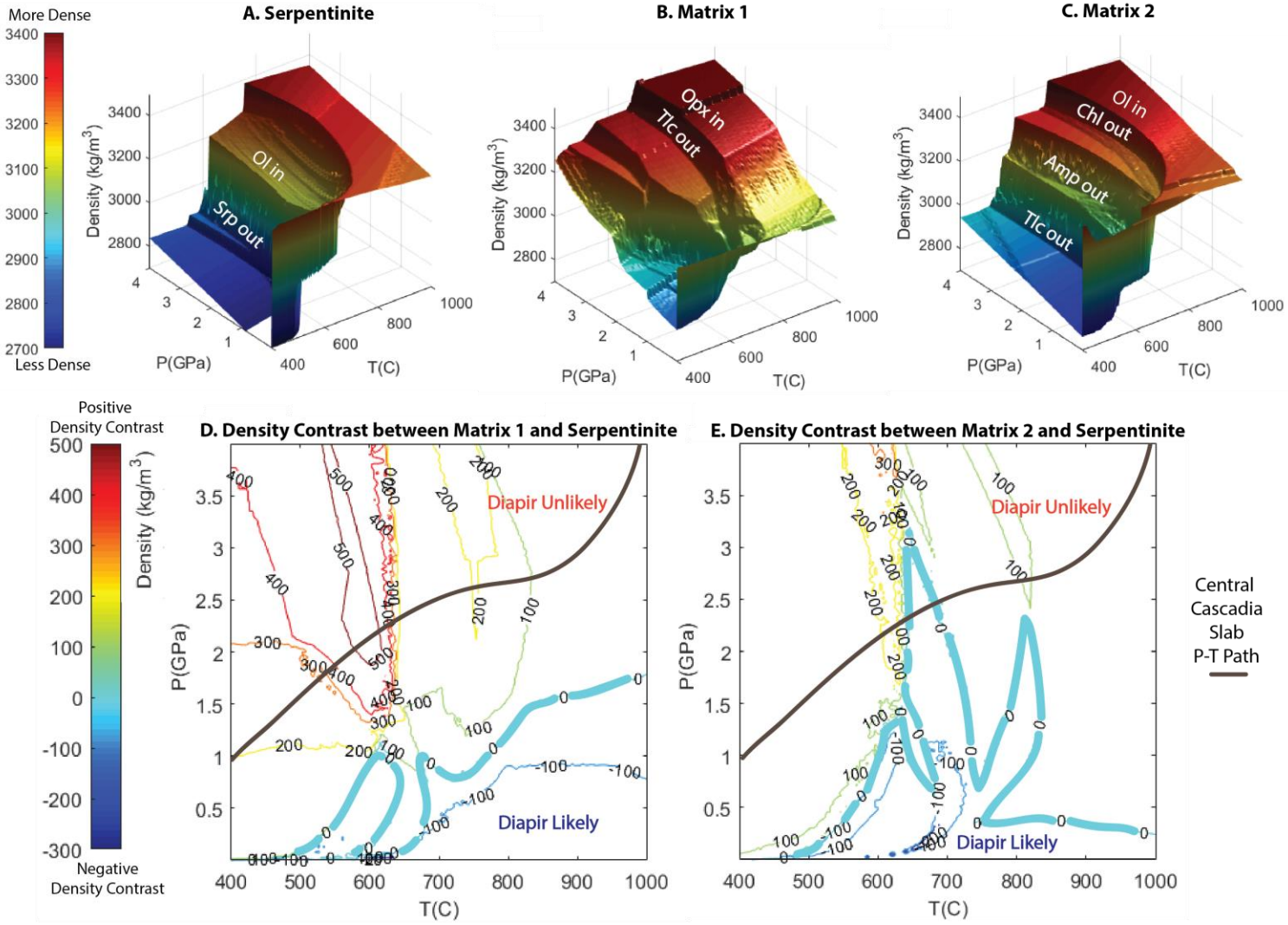

Figure 10: The calculated densities for Serpentinite (A), Matrix 1 (B), and Matrix 2 (C) are plotted as a function of pressure and temperature. The step-like patterns are based on stable mineral assemblages within each pressure and temperature field. Labeled on the major steps are where phases become unstable (out) or more stable (in) along a subduction prograde path. The density contrast between Matrix 1 and Serpentinite (D) and that of Matrix 2 and Serpentinite (E) are shown in contour plots. Slab pressure-temperature paths of Central Cascadia were superimposed (Syracuse et al., 2010).

Density changes as a function of pressure and temperature based on the mineral assemblages and abundances present. Changes in phase stability primarily caused by changes in temperature causes abrupt changes in density, causing the step-like pattern in Figures 10A, 10B, and 10C. The presence of pyroxenes at higher temperatures and pressures in all models contribute to larger densities at these conditions. Olivine-bearing mineral assemblages of Serpentinite and Matrix 2 at higher temperatures also cause larger density values that decrease dramatically as serpentine becomes the abundant phase over olivine at lower temperature. Matrix 1 and Matrix 2 densities decrease as talc becomes a stable phase. The density contrast between Matrix 1 and Serpentinite and that of Matrix 2 and Serpentinite were graphed in contour plots (Figure 10D, 10E). The 0-contour line represents the divide between pressure and temperature regions where diapir formation is likely or unlikely. Regions with a negative density contrast have density contrast values below zero and are dark blue in color. Diapir formation is possible under pressure and temperature conditions that cause a negative density contrast. Regions with a positive density contrast have density contrast values above zero and diapir formation is unlikely to occur at these regions. Subduction slab top pressure and temperature paths of Central Cascadia were superimposed on the density contrast contour plots (Syracuse et al., 2010). These pressure-temperature paths were chosen because the Catalina Schist is a hot subduction zone and thus, would be likely to have a similar pressure-temperature path as that of Cascadia. Pressure-temperature paths do not cross regions of likely diapir formation in Figure 10D, indicating that diapir formation is not likely at subduction conditions between interfaces with Matrix 1 and Serpentinite compositions. However, pressure and temperature paths do cross regions of likely diapir formation in Figure 10E within temperatures and pressures of 644 – 676 °C and 2.3 – 2.4 GPa, respectively.

Geodynamic Modeling

Density contrast, viscosity, thickness, and wavelength are directly related to diapir growth time and a growth rate curve (Figure 11) can be created based on Equation 1, Equation 2, and Equation 3 from Turcotte and Schubert (2014) to show regions where diapir formation is likely to occur.

$$T \rightarrow \frac{24\mu}{(\rho 1 - \rho 2)gb}\left(\frac{\lambda}{2\pi b}\right)^2$$

Equation 1: Diapir growth time for large wavelengths.

$$T \rightarrow \frac{4\mu}{(\rho 1 - \rho 2)gb}\left(\frac{2\pi b}{\lambda}\right)$$

Equation 2: Diapir growth time for small wavelengths.

$$T = \frac{\left(\frac{4\mu}{(\rho 1 - \rho 2)gb}\right)\left(\frac{\lambda}{2\pi b} + \frac{1}{sinh\left(\frac{2\pi b}{\lambda}\right)cosh\left(\frac{2\pi b}{\lambda}\right)}\right)}{\left(\frac{\lambda}{2\pi b}\right)^2 \tanh\left(\frac{2\pi b}{\lambda}\right) - \frac{1}{sinh\left(\frac{2\pi b}{\lambda}\right)cosh\left(\frac{2\pi b}{\lambda}\right)}}$$

Equation 3: Diapir growth time for any wavelength.

Wave number is $\frac{2\pi b}{\lambda}$. The variable b is mélange thickness and λ is wavelength. The variable μ is viscosity, and the variables ρ1 and ρ2 refer to the densities of the two materials at the interface. T refers to diapir growth time and g is the gravitational acceleration. Diapir formation is more likely to occur for a smaller growth time, and less likely to occur for a greater growth time. Long wavelengths and short wavelengths affect diapir growth time differently and can be calculated based on Equation 1 and Equation 2, respectively. There exists a wave number at which diapir growth takes the least amount of time where the effects of long wavelengths and short wavelengths on material movement and shearing are both minimized and is represented by Equation 3.

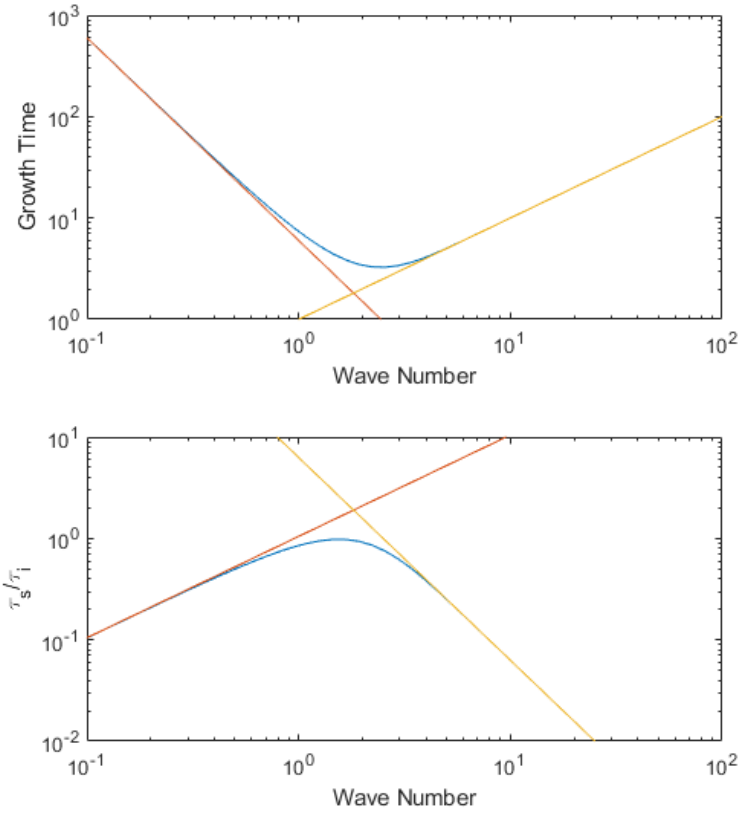

Figure 11: The growth rate curve of dimensionless wave number and dimensionless growth time is shown in the top plot and the growth rate curve of dimensionless wave number and the proportion of slab time (τ_s) to diapir growth time (τ_i) is shown in the bottom plot. The red lines represent long wavelengths and the yellow lines represent short wavelengths. The MATLAB script for these plots is in Figure 2 of the Appendix.

The bottom of the blue curve in the top plot of Figure 11 represents where diapir formation is most likely to occur. Diapir formation is most likely to occur when slab time (τ_s) is larger than diapir growth time (τ_i). A larger slab time means a slower slab velocity, which would be less likely to cause entrainment of a diapir. Therefore, the largest ratio of τ_s/τ_i represents where diapir formation is most likely to occur and is represented by the top of the curve in the bottom plot of Figure 11.

Density contrast values were calculated with Perple_X and range from 18 – 51 kg/m^3. The Central Cascadia pressure and temperature conditions associated with each density contrast value are listed in Table 4 of the Appendix. Other parameters that control diapir formation were selected based on prior research (Table 4). 50 – 1000 m mélange thicknesses were selected and are based on the kilometer-scale size of mélange zones found at the Catalina Schist (Bebout and Barton, 2002) as well as the estimated average thickness of subducted sediments for Central Cascadia (Syracuse et al., 2010). Viscosities of 10^{18} – 10^{19} Pa-s were based on the estimated viscosities of serpentinized mantle and mélange (Grigull et al., 2012).

Parameters	Values
Density Contrast ($\rho 1 - \rho 2$)	18 – 51 kg/m^3
Mélange Thickness (b)	50 – 1000 m
Viscosity (μ)	10^{18} – 10^{19} Pa-s
Slab Velocity	30 km/Ma
Slab Dip	19.8 degrees
Slab Time	0.41 Ma

Table 4: The parameters for calculating diapir growth time.

Length of the slab window depth interval for which there is a negative density contrast between Matrix 2 and Serpentinite was calculated using trigonometry (Figure 12). Slab time was calculated based on the length of the slab velocity and dip of Central Cascadia (Syracuse et al., 2010).

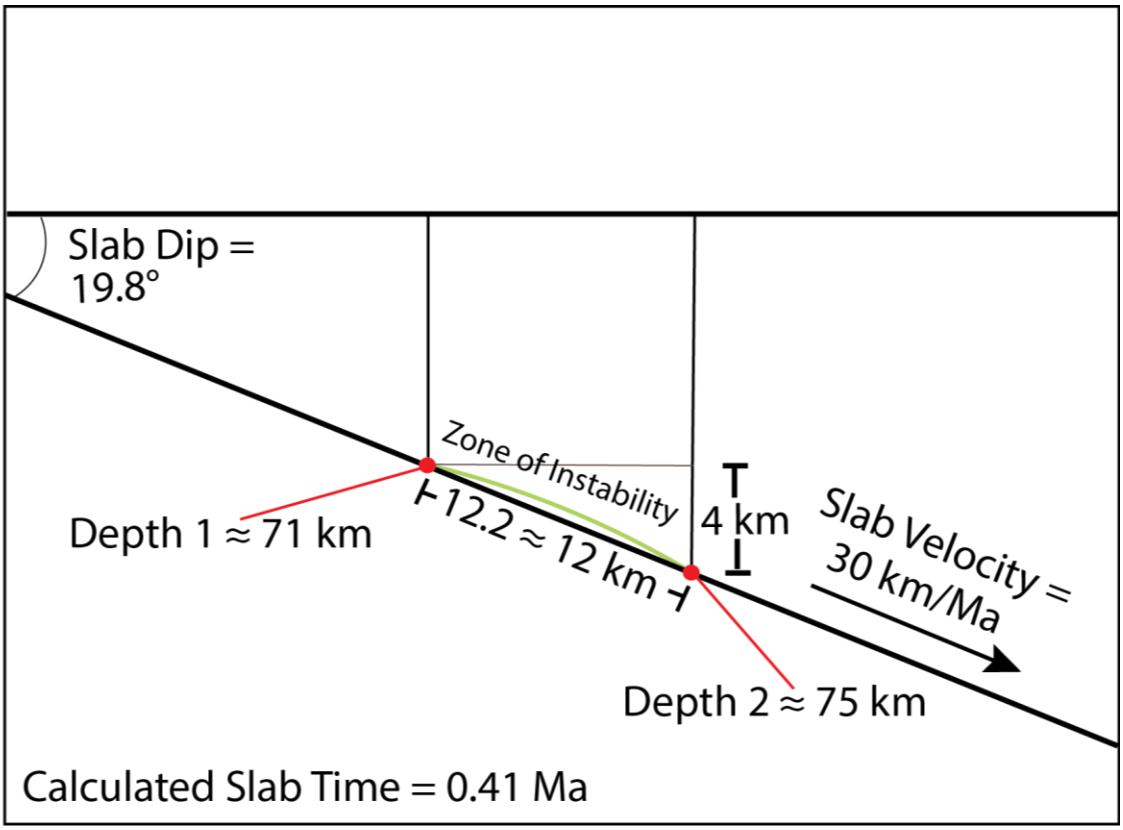

Figure 12: The difference between the minimum (Depth 1) and maximum (Depth 2) depths for which there is a negative density contrast between Matrix 2 and Serpentinite is about 4 km. 4/sin(19.8) = 12 km, the length of the slab window depth interval. This length divided by the slab velocity results in 0.41 Ma, the slab time.

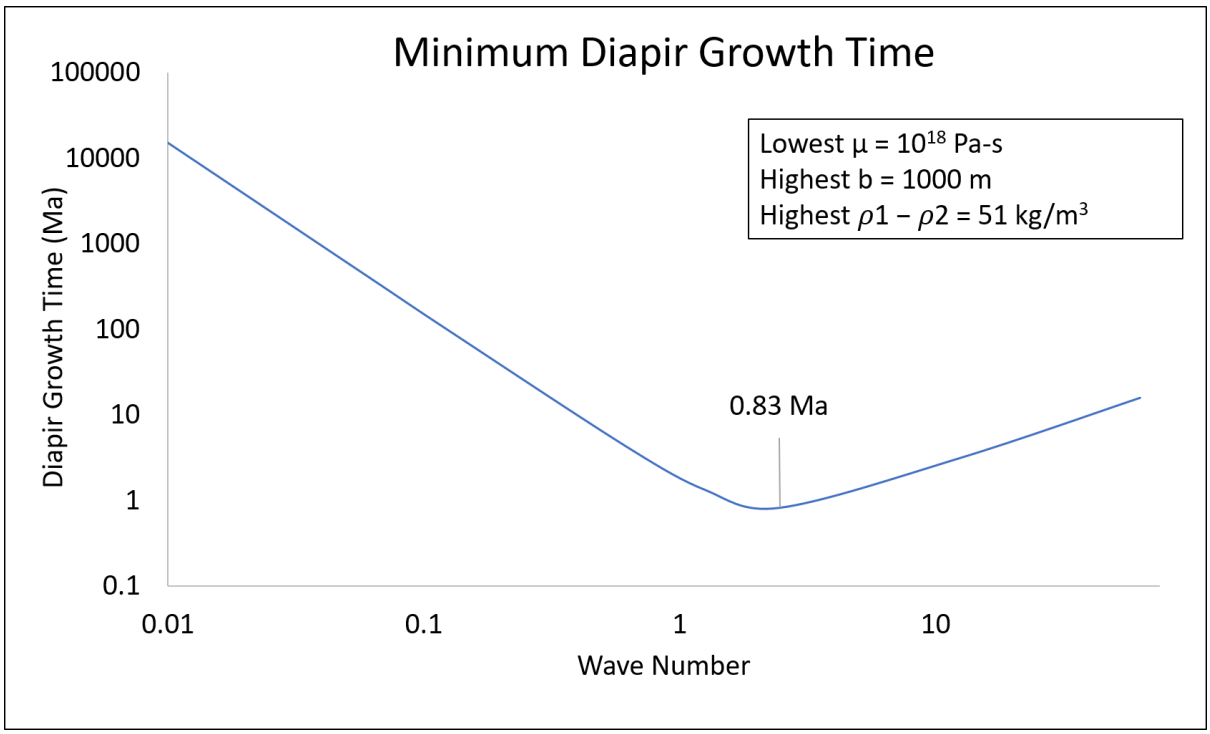

Figure 13: Diapir growth time calculated at a viscosity of 10^{18} Pa-s, mélange thickness of 1000 m, and density contrast of 51 kg/m^3. The smallest value for growth time is 0.83 Ma at a wave number of 2.4 and wavelength of 2570 m.

Diapir formation is more likely to occur for smaller growth times caused by lower viscosities, larger density contrasts, and thicker mélange. Diapir growth time was calculated for conditions at which diapir growth time would be smallest. 0.83 Ma is the smallest diapir growth time possible within the parameters. The smallest diapir growth time is larger than the calculated slab time of 0.41 Ma, indicating that the slab moves too rapidly for Matrix 2 to rise at the slab interface and form a diapir.

Conclusion

The two samples of mélange matrix collected for this study have differing mineralogies. Matrix 1 was found to be rich in biotite, chlorite, and clinoamphibole, whereas Matrix 2 was found to be rich in orthopyroxene and talc. Perple_X models produced mineral assemblages that matched the observed mineral assemblages moderately well for the pressure and temperature conditions recorded by the samples. According to the Perple_X models, Matrix 1 will always be more dense than Serpentinite along the entire pressure and temperature path of Central Cascadia, indicating that Matrix 1 would be unlikely to form a diapir at any point during subduction. There is a narrow window of ~12 km along the Central Cascadia slab at pressures of 2.3 – 2.4 GPa and temperatures of 644 – 676 °C for which Matrix 2 would be less dense than the overlying Serpentinite, creating conditions favorable for diapir formation. High density contrast, low viscosity, and large mélange thickness are factors that decreased diapir growth time and created the most optimal conditions for diapir formation. Calculations comparing growth time of diapir formation to the time the subducting slab would move through the window of pressure and temperature conditions for diapir formation indicate that the slab will move too quickly through this window for a diapir to form and rise. Thus, the formation of diapirs from mélange at the slab interface was determined to be unlikely.

Acknowledgments

I would like to thank Dr. Sarah Penniston-Dorland, Kayleigh Harvey, and Dr. Laurent Montési for their expertise and guidance throughout this interdisciplinary project. I would also like to thank Dr. Stanley A. Mertzman for collecting the XRF data at Franklin and Marshall College and the Catalina Island Conservancy for their permission to conduct field work. The research was funded by the Senior Thesis Grant and by the National Science Foundation Grant EAR-1419871.

References

Andersen, D. J., & Lindsley, D. H. (1988). Internally consistent solution models for Fe-Mg-Mn-Ti oxides; Fe-Ti oxides. *American Mineralogist*, *73*(7-8), 714-726.

Bebout, G. E., & Barton, M. D. (1989). Fluid flow and metasomatism in a subduction zone hydrothermal system: Catalina Schist terrane, California. *Geology*, *17*(11), 976-980.

Bebout, G. E., & Barton, M. D. (2002). Tectonic and metasomatic mixing in a high-T, subduction-zone mélange—insights into the geochemical evolution of the slab–mantle interface. *Chemical Geology*, *187*(1-2), 79-106.

Bebout, G. E., & Penniston-Dorland, S. C. (2016). Fluid and mass transfer at subduction interfaces—The field metamorphic record. *Lithos*, *240*, 228-258.

Behn, M. D., Kelemen, P. B., Hirth, G., Hacker, B. R., & Massonne, H. J. (2011). Diapirs as the source of the sediment signature in arc lavas. *Nature Geoscience*, *4*(9), 641.

Connolly, J. A. D. (2009). The geodynamic equation of state: what and how. *Geochemistry, Geophysics, Geosystems*, *10*(10).

Diener, J. F. A., Powell, R., White, R. W., & Holland, T. J. B. (2007). A new thermodynamic model for clino-and orthoamphiboles in the system Na2O–CaO–FeO–MgO–Al2O3–SiO2–H2O–O. *Journal of Metamorphic Geology*, *25*(6), 631-656.

Elliott, T. (2003). Tracers of the slab. *Geophysical Monograph-American Geophysical Union*, *138*, 23-46.

Gerya, T. V., & Yuen, D. A. (2003). Rayleigh–Taylor instabilities from hydration and melting propel 'cold plumes' at subduction zones. *Earth and Planetary Science Letters*, *212*(1-2), 47-62.

Hall, P. S., & Kincaid, C. (2001). Diapiric flow at subduction zones: A recipe for rapid transport. *Science*, *292*(5526), 2472-2475.

Hasenclever, J., Morgan, J. P., Hort, M., & Rüpke, L. H. (2011). 2D and 3D numerical models on compositionally buoyant diapirs in the mantle wedge. *Earth and Planetary Science Letters*, *311*(1-2), 53-68.

Holland, T. J. B., & Powell, R. (2011). An improved and extended internally consistent thermodynamic dataset for phases of petrological interest, involving a new equation of state for solids. *Journal of Metamorphic Geology*, *29*(3), 333-383.

Jennings, E. S., & Holland, T. J. (2015). A simple thermodynamic model for melting of peridotite in the system NCFMASOCr. *Journal of Petrology*, *56*(5), 869-892.

Marschall, H. R., & Schumacher, J. C. (2012). Arc magmas sourced from mélange diapirs in subduction zones. *Nature Geoscience*, *5*(12), 862.

McCulloch, M. T., & Gamble, J. A. (1991). Geochemical and geodynamical constraints on subduction zone magmatism. *Earth and Planetary Science Letters*, *102*(3-4), 358-374.

Miller, N. C., & Behn, M. D. (2012). Timescales for the growth of sediment diapirs in subduction zones. *Geophysical Journal International*, *190*(3), 1361-1377.

Nielsen, S. G., & Marschall, H. R. (2017). Geochemical evidence for mélange melting in global arcs. *Science Advances*, *3*(4), e1602402.

Padrón-Navarta, J. A., Sánchez-Vizcaíno, V. L., Hermann, J., Connolly, J. A., Garrido, C. J., Gómez-Pugnaire, M. T., & Marchesi, C. (2013). Tschermak's substitution in antigorite and consequences for phase relations and water liberation in high-grade serpentinites. *Lithos*, *178*, 186-196.

Penniston-Dorland, S. C., Kohn, M. J., & Piccoli, P. M. (2018). A mélange of subduction temperatures: Evidence from Zr-in-rutile thermometry for strengthening of the subduction interface. *Earth and Planetary Science Letters*, *482*, 525-535.

Platt, J.P., (1976). The significance of the Catalina Schist in the history of the southern California borderland, in Howell, D.G., ed., *Aspects of the Geologic History of the California Continental Borderland: Pacific Section*, American Association of Petroleum Geologists, Miscellaneous Publication 24, 47–52.

Powell, R., & Holland, T. (1999). Relating formulations of the thermodynamics of mineral solid solutions; activity modeling of pyroxenes, amphiboles, and micas. *American Mineralogist*, *84*(1-2), 1-14.

Sorensen, S. S., & Barton, M. D. (1987). Metasomatism and partial melting in a subduction complex Catalina Schist, southern California. *Geology*, *15*(2), 115-118.

Syracuse, E. M., van Keken, P. E., & Abers, G. A. (2010). The global range of subduction zone thermal models. *Physics of the Earth and Planetary Interiors*, *183*(1-2), 73-90.

Turcotte, D., & Schubert, G. (2014). *Geodynamics*. Cambridge University Press.

van Keken, P. E., Hacker, B. R., Syracuse, E. M., & Abers, G. A. (2011). Subduction factory: 4. Depth-dependent flux of H2O from subducting slabs worldwide. *Journal of Geophysical Research: Solid Earth*, *116*(B1).

Weaver, B. L. (1991). The origin of ocean island basalt end-member compositions: trace element and isotopic constraints. *Earth and Planetary Science Letters*, *104*(2-4), 381-397.

Wei, C., & Powell, R. (2003). Phase relations in high-pressure metapelites in the system KFMASH (K 2 O–FeO–MgO–Al 2 O 3–SiO 2–H 2 O) with application to natural rocks. *Contributions to Mineralogy and Petrology*, *145*(3), 301-315.

White, R. W., Powell, R., & Johnson, T. E. (2014). The effect of Mn on mineral stability in metapelites revisited: New a–x relations for manganese-bearing minerals. *Journal of Metamorphic Geology*, *32*(8), 809-828.

Whitney, D. L., & Evans, B. W. (2010). Abbreviations for names of rock-forming minerals. *American Mineralogist*, *95*(1), 185-187

Zhu, G., Gerya, T. V., Yuen, D. A., Honda, S., Yoshida, T., & Connolly, J. A. (2009). Three-dimensional dynamics of hydrous thermal-chemical plumes in oceanic subduction zones. *Geochemistry, Geophysics, Geosystems*, *10*(11).

Appendix

Specimen	Serpentinite	Matrix 1	Matrix 2
SiO_2	46.33	52.76	52.08
TiO_2	0.05	0.86	0.09
$Al2O_3$	2.32	9.49	4.87
Fe_2O_3(T)	8.29	11.46	7.75
MnO	0.11	0.20	0.10
MgO	41.89	17.25	33.41
CaO	0.03	5.07	0.56
Na_2O	0.04	1.06	0.15
K_2O	0.01	0.75	0.05
P_2O_5	0.01	0.17	0.01
Total	99.08	99.07	99.07
LOI	13.63	5.69	5.77
FeO	1.17	6.15	5.37
Fe_2O_3	6.99	4.63	1.78
Rb	<0.5	36.1	<0.5
Sr	1	26	<1
Y	<0.5	31.5	0.6
Zr	8	117	8
V	39	166	69
Ni	2369	786	1781
Cr	2789	1177	4033
Nb	<0.5	11.6	<0.5
Ga	1.3	11.6	5.2
Cu	<2	13	31
Zn	46	123	48
Co	106	59	95
Ba	29	312	22
La	<2	17	<2
Ce	<2	29	<2
U	<0.5	<0.5	<0.5
Th	<0.5	3.3	<0.5
Sc	10	19	10
Pb	<1	2	<1

Table 1A: The bulk rock composition of each sample obtained through XRF analysis. Oxides are in wt% and elements are in ppm.

Specimen	Mean	Standard Deviation	Coefficient of variation (%)
SiO_2	49.82	0.2076	0.4200
TiO_2	2.71	0.00873	0.320
Al_2O_3	13.39	0.08635	0.6400
Fe_2O_3(T)	12.43	0.1433	1.150
MnO	0.167	0.000702	0.420
MgO	7.12	0.0361	0.510
CaO	11.42	0.03480	0.3000
Na_2O	2.154	0.02512	1.170
K_2O	0.506	0.00295	0.580
P_2O_5	0.275	0.00234	0.850
Total	99.99	0.3845	0.3800
Rb	7.9	0.48	6.1
Sr	380	3.88	1.02
Y	25.66	0.3098	1.210
Zr	166.8	2.044	1.230
V	326.3	2.406	0.7400
Ni	122.1	0.7379	0.6000
Cr	321.3	10.12	3.150
Nb	17.02	0.4467	2.620
Ga	17.87	0.1418	0.7900
Cu	126	3.68	2.92
Zn	91.5	0.527	0.580
Co	45.6	1.17	2.57
Ba	116	7.60	6.55
La	15.8	1.32	8.35
Ce	29.2	0.919	3.15
U	1.29	0.507	39.3
Th	0.8	0.5	60
Sc	33.7	0.675	2.00
Pb	1.2	0.42	35

Table 1B: The mean, standard deviation, and coefficient of variations for XRF data were calculated using BHVO standards. Oxides are in wt% and trace elements are in ppm.

Solution Models	Phase	References
Atg(PN)	Serpentine	Padrón-Navarta et al., 2013
Bio(HP)	Biotite	Powell and Holland, 1999
Chl(W)	Chlorite	White et al., 2014
Cpx(HP)	Clinopyroxene	Jennings and Holland, 2015
GlTrTsPg	Clinoamphibole	Wei and Powell, 2003
Gt(HP)	Garnet	Powell and Holland, 1999
IlHm(A)	Ilmenite	Andersen et al., 1988
MF	Magnetite	Powell and Holland, 1999
O(HP)	Olivine	Powell and Holland, 1999
oAmph(DP)	Orthoamphibole	Diener et al., 2007
Opx(HP)	Orthopyroxene	Powell and Holland, 1999

Table 2: Phases and references associated with each Perple_X solution model.

Sample and Mineral	SiO_2	TiO_2	Al_2O_3	FeO	MnO	MgO	CaO	Na_2O	K_2O	Total
Matrix 1 Biotite 4	42.47	1.04	17.54	9.49	0.06	18.04	0.13	0.17	4.09	93.16
Matrix 1 Biotite 4	41.59	1.14	17.35	10.71	0.08	17.12	0.29	0.25	4.38	93.08
Matrix 1 Biotite 3	42.49	1.03	17.60	9.73	0.10	17.67	0.26	0.21	4.21	93.47
Matrix 1 Biotite 3	42.30	1.10	17.34	9.85	0.11	17.94	0.35	0.18	3.71	93.03
Matrix 1 Biotite 1	40.59	1.04	16.40	11.43	0.11	18.06	0.33	0.08	0.88	89.09
Matrix 1 Biotite 1	43.08	1.06	17.28	9.41	0.08	19.96	0.23	0.02	0.12	91.42
Matrix 1 Biotite 2	39.31	1.09	16.42	8.93	0.08	18.11	0.36	0.16	3.83	88.47
Matrix 1 Biotite 2	39.92	1.03	16.48	10.55	0.09	18.14	0.37	0.30	3.98	91.00
Matrix 1 Amphibole 1	50.56	0.29	10.02	8.14	0.26	16.20	10.72	2.05	0.10	98.54
Matrix 1 Amphibole 1	52.26	0.19	8.07	7.82	0.38	16.63	10.90	1.73	0.25	98.32
Matrix 1 Amphibole 1	59.35	0.16	2.80	5.82	0.05	26.35	0.06	0.30	0.33	95.22
Matrix 1 Amphibole 1	59.14	0.17	4.01	5.91	0.05	24.82	0.14	0.31	0.39	94.94
Matrix 1 Amphibole 2	48.72	0.43	11.75	7.72	0.18	16.65	10.45	2.06	0.12	98.26
Matrix 1 Amphibole 2	50.39	0.35	10.15	7.55	0.16	17.17	10.61	1.90	0.11	98.58
Matrix 1 Amphibole 3	48.76	0.44	12.40	7.88	0.28	15.59	10.85	2.40	0.14	99.00
Matrix 1 Amphibole 3	48.17	0.45	13.61	7.67	0.21	15.82	10.67	2.30	0.17	99.23
Matrix 1 Amphibole 4	48.00	0.44	13.50	7.76	0.18	15.64	10.85	2.24	0.17	98.86
Matrix 1 Amphibole 4	49.55	0.38	11.27	8.10	0.19	16.67	9.99	1.74	0.13	98.02
Matrix 1 Talc 2	56.11	0.16	5.19	6.71	0.06	24.09	0.07	0.15	1.00	93.54
Matrix 1 Talc 2	59.48	0.05	3.00	6.20	0.02	25.34	0.06	0.15	0.40	94.79

Sample and Mineral	SiO_2	TiO_2	Al_2O_3	FeO	MnO	MgO	CaO	Na_2O	K_2O	Total
Matrix 1 Chlorite 1	31.68	0.14	21.38	11.80	0.13	22.33	0.22	0.05	0.12	88.07
Matrix 1 Chlorite 1	32.28	0.10	20.20	12.02	0.18	22.62	0.21	0.02	0.03	87.83
Matrix 1 Chlorite 2	49.16	0.75	10.90	7.63	0.07	21.38	0.19	0.19	2.06	92.37
Matrix 1 Chlorite 2	56.14	0.40	6.20	6.52	0.06	23.43	0.14	0.19	1.05	94.14
Matrix 2 Orthopyroxene 2	57.99	BDL	0.36	7.51	0.11	34.55	0.08	BDL	BDL	100.71
Matrix 2 Orthopyroxene 2	57.84	0.03	0.41	7.50	0.12	34.91	0.08	BDL	BDL	101.03
Matrix 2 Orthopyroxene 3	58.12	0.04	0.19	7.30	0.12	34.86	0.09	BDL	0.01	100.80
Matrix 2 Orthopyroxene 3	58.21	0.03	0.16	7.26	0.13	35.15	0.10	BDL	BDL	101.07
Matrix 2 Orthopyroxene 4	57.70	0.06	0.15	7.17	0.14	34.91	0.10	BDL	0.01	100.29
Matrix 2 Orthopyroxene 4	57.98	BDL	0.22	7.04	0.12	34.67	0.07	BDL	0.02	100.16
Matrix 2 Orthopyroxene 5	57.68	0.05	0.12	8.05	0.21	34.53	0.07	BDL	BDL	100.77
Matrix 2 Orthopyroxene 5	57.93	0.08	0.16	7.53	0.13	34.65	0.08	BDL	0.01	100.68
Matrix 2 Orthopyroxene 6	58.09	0.03	0.24	7.39	0.09	34.49	0.05	BDL	0.02	100.46
Matrix 2 Orthopyroxene 6	57.65	0.05	0.33	7.55	0.16	34.60	0.05	BDL	0.01	100.48
Matrix 2 Orthopyroxene 7	58.27	0.05	0.19	7.00	0.12	34.93	0.06	BDL	BDL	100.72
Matrix 2 Orthopyroxene 7	58.75	0.03	0.16	7.04	0.10	34.39	0.06	BDL	0.02	100.66
Matrix 2 Orthopyroxene 8	57.81	0.07	0.12	8.28	0.13	34.15	0.07	BDL	0.01	100.68
Matrix 2 Orthopyroxene 9	57.96	BDL	0.20	7.20	0.15	34.27	0.09	BDL	0.01	99.92
Matrix 2 Orthopyroxene 9	58.05	0.05	0.18	7.92	0.14	34.46	0.07	BDL	BDL	100.94
Matrix 2 Talc 1	63.15	0.08	0.05	1.59	BDL	30.29	BDL	BDL	0.02	95.19
Matrix 2 Talc 1	63.35	0.07	0.02	1.52	0.02	30.48	0.03	0.02	BDL	95.53
Matrix 2 Chlorite 1	31.82	0.04	17.01	3.79	BDL	32.09	BDL	BDL	0.01	86.41
Matrix 2 Chlorite 1	32.34	0.09	15.82	3.85	BDL	33.10	BDL	0.03	0.01	86.71
Matrix 2 Chlorite 2	31.32	0.12	16.72	3.88	0.03	32.04	BDL	BDL	BDL	85.78
Matrix 2 Chlorite 2	31.82	0.04	17.18	3.94	BDL	32.23	0.02	BDL	0.02	86.94
Matrix 2 Talc 2	44.98	0.07	0.26	10.59	0.25	31.41	0.05	0.02	0.05	87.78
Matrix 2 Talc 2	46.13	0.04	0.16	10.16	0.23	32.73	0.04	0.06	0.02	89.61
Serpentinite Srp #1	43.98	BDL	BDL	2.00	0.02	39.61	0.02	BDL	BDL	85.63
Serpentinite Srp #2	43.94	BDL	BDL	1.95	0.05	40.05	BDL	BDL	BDL	86.01
Serpentinite Srp #3	44.08	BDL	BDL	2.11	0.03	39.92	0.03	BDL	0.03	86.21
Serpentinite Srp #4	44.13	BDL	0.03	2.16	0.03	39.76	0.02	BDL	0.01	86.17

Sample and Mineral	SiO_2	TiO_2	Al_2O_3	FeO	MnO	MgO	CaO	Na_2O	K_2O	Total
Serpentinite Vein #1	44.53	BDL	0.03	4.40	0.11	35.69	0.05	BDL	0.07	84.88
Serpentinite Vein #1	44.46	BDL	0.02	4.47	0.11	35.98	0.04	BDL	0.03	85.13
Serpentinite Vein #2	44.01	BDL	BDL	5.27	0.19	33.55	0.07	BDL	0.06	83.19
Serpentinite Vein #2	44.24	BDL	0.03	4.67	0.12	35.21	0.06	BDL	0.05	84.43
Serpentinite Vein #3	44.84	BDL	BDL	3.78	0.06	36.10	0.03	BDL	0.03	84.88
Serpentinite Vein #3	45.64	BDL	0.02	6.09	0.11	30.66	0.11	BDL	0.16	82.79
Serpentinite Vein #4	44.24	0.03	BDL	4.45	0.11	35.94	0.03	BDL	0.03	84.87
Serpentinite Vein #4	44.32	BDL	0.03	4.16	0.14	36.37	0.04	0.02	0.02	85.12
Serpentinite Chlorite #1	32.00	BDL	15.69	2.58	0.03	32.63	0.02	BDL	BDL	85.46
Sepentinite Chlorite #1	31.90	0.11	16.08	2.73	0.02	32.81	BDL	BDL	BDL	86.17
Serpentinite Chlorite #2	31.76	0.12	15.50	2.52	BDL	32.75	BDL	0.03	0.01	85.34
Serpentinite Chlorite #2	32.19	0.12	15.32	2.56	0.02	33.12	BDL	BDL	BDL	85.59

Table 3: EPMA data of the minerals analyzed in wt% oxides. Values below the detection limit are marked as BDL.

T (°C)	P (GPa)	Depth (km)	Density Contrast (kg/m^3)
644	2.3	70.6	49
647	2.3	71.1	49
651	2.3	71.7	49
655	2.4	72.2	50
658	2.4	72.7	51
663	2.4	73.2	47
667	2.4	73.7	35
671	2.4	74.2	18
676	2.4	74.8	19

Table 4: Central Cascadia slab top temperature and pressure conditions as well as depths (Syracuse et al., 2010) under which Matrix 2 is less dense than Serpentinite. Density contrasts were calculated using Perple_X.

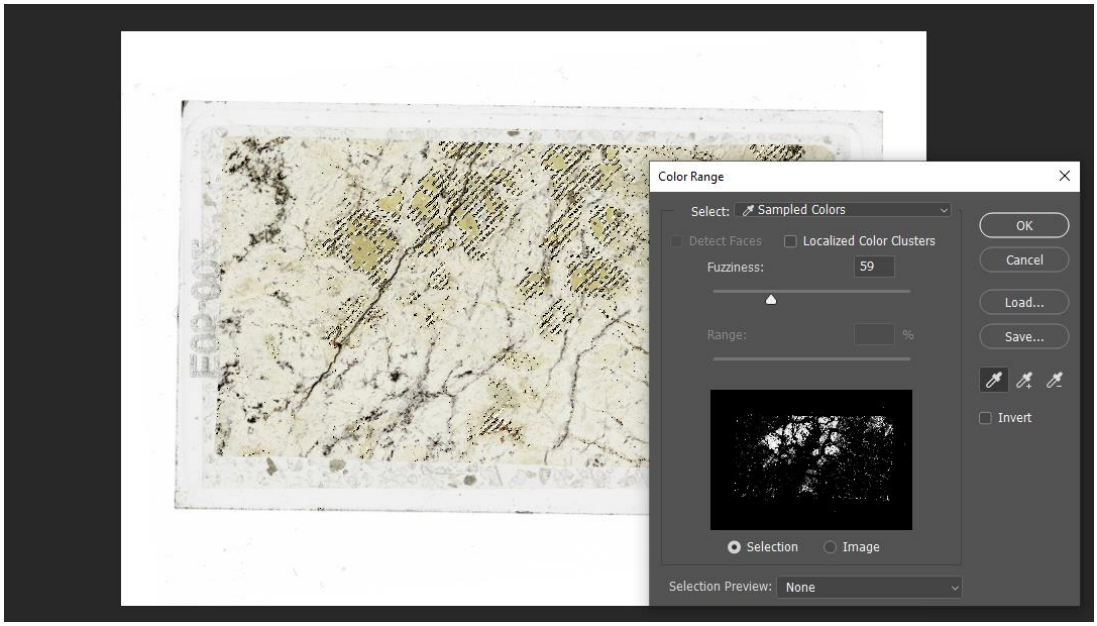

Figure 1: Olivine pseudomorphs selected in the thin section scan of Serpentinite on Adobe Photoshop. The color range tool was used in combination with the magic wand tool to select a phase and count the number of pixels, which can be divided by the total number of pixels in the thin section to determine mineral percentages.

```
k = logspace(-1,2);
%Ti is diapir growth time
Ti = (((1./k)+(1./(sinh(k).*cosh(k)))./(((1./k).^2).*tanh(k)-(1./((sinh(k).*cosh(k))))))
%Ts is slab time
Ts = 2*pi./k;

figure(1); clf;

subplot 211; hold on
loglog(k,Ti); %Equation 6.158
loglog(k,6*k.^(-2))  % Equation 6.159
loglog(k,k) %Equation 6.160

set(gca,'XScale','log','YScale','log');
box on;
xlabel('Wave Number')
ylabel('Growth Time')
xlim([0.1 100])
ylim([1 1000])

subplot 212; hold on;
loglog(k,Ts./Ti)
loglog(k,k*pi/3)
loglog(k,2*pi./(k.^2))

set(gca,'XScale','log','YScale','log');
box on;
xlabel('Wave Number')
ylabel('\tau_s/\tau_i')
ylim([0.01,10])
```

Figure 2: MATLAB script for diapir growth curves in Figure 11.

Honor Code

I pledge on my honor that I have not given or received any unauthorized assistance or plagiarized on this assignment.

_____

Cristy Quynh Ho